

Curl-Flow: Pointwise Incompressible Velocity Interpolation for Grid-Based Fluids

JUMYUNG CHANG, University of Waterloo
VINICIUS C. AZEVEDO, ETH Zurich
CHRISTOPHER BATTY, University of Waterloo

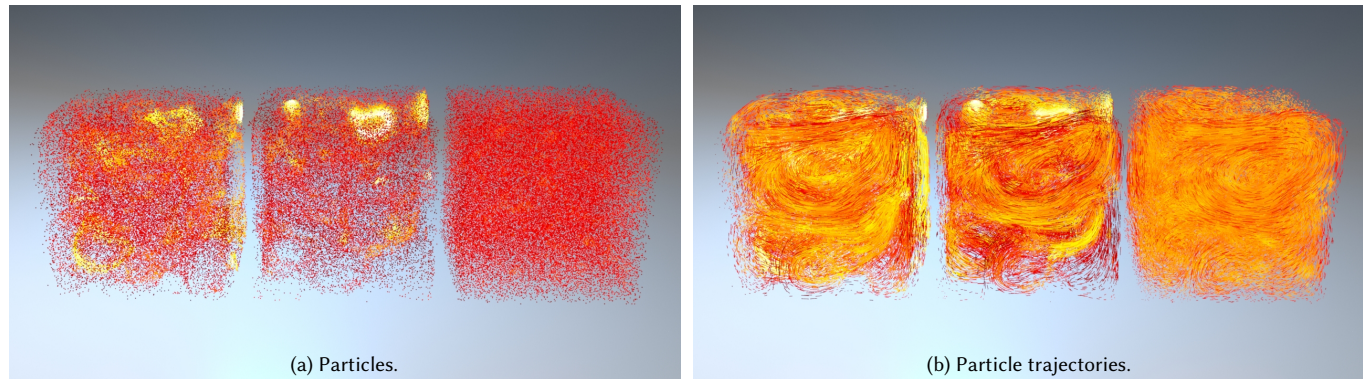


Fig. 1. **Effect of Interpolants on Particle Distribution in 3D:** The results of identical, initially uniform particle distributions advected through the same $5 \times 5 \times 5$ discretely incompressible field for 300 frames using different velocity interpolants. In each trio, left is standard trilinear velocity interpolation, center is monotonic cubic velocity interpolation [Fritsch and Carlson 1980], and right is our Curl-Flow method. The coloring indicates the per-particle local density estimate, with yellow/white being highest density. Standard velocity interpolants lead to undesirable severe clustering and spreading, while our pointwise incompressible Curl-Flow interpolation preserves close to uniform particle distributions over long periods.

We propose a novel methodology to enhance grid-based fluid animation with *pointwise* divergence-free velocity interpolation. Our method takes as input a discretely divergence-free staggered grid velocity field generated by a standard pressure projection, and first recovers a consistent corresponding edge-based discrete vector potential in 3D (or node-based stream function in 2D). We interpolate these values to form a pointwise potential, and apply the *continuous* curl operator to recover a pointwise flow field that is perfectly incompressible. Our method supports irregular geometry through the use of level set-based cut-cells. To recover a smooth and velocity-consistent discrete vector potential in 3D, we employ a sweeping approach followed by a gauge correction that requires a single scalar Poisson solve, rather than a vector Poisson problem. In both 2D and 3D, we show how modified interpolation strategies can be applied to better account for the presence of irregular cut-cell boundaries. Our results demonstrate that our overall proposed *Curl-Flow* framework produces significantly better particle trajectories that suffer from far fewer spurious sources or sinks, respect irregular obstacles, and better preserve particle distributions over time.

CCS Concepts: • **Computing methodologies** → **Physical simulation**.

Additional Key Words and Phrases: divergence-free, stream function, vector potential, velocity interpolation, advection

Authors' addresses: Jумыung Chang, University of Waterloo; Vinicius C. Azevedo, ETH Zurich; Christopher Batty, University of Waterloo.

© 2021
0730-0301/2021/4-ART0 \$15.00
<https://doi.org/10.1145/nnnnnnnn.nnnnnnnn>

ACM Reference Format:

Jумыung Chang, Vinicius C. Azevedo, and Christopher Batty. 2021. Curl-Flow: Pointwise Incompressible Velocity Interpolation for Grid-Based Fluids. *ACM Trans. Graph.* 0, 0, Article 0 (April 2021), 15 pages. <https://doi.org/10.1145/nnnnnnnn.nnnnnnnn>

1 INTRODUCTION

The assumption of incompressibility is pervasive in computer animation of fluids. Since compressive effects are imperceptible in many (but of course not all) visually relevant liquid and gas scenarios, neglecting fast-moving compression waves is often justified in practice and yields significant efficiency gains. Mathematically, incompressibility implies that the fluid velocity field \mathbf{u} should be divergence-free: $\nabla \cdot \mathbf{u} = 0$. Popular staggered grid-based schemes rely on this assumption and use finite difference, finite volume, or discrete exterior calculus ideas to transform the continuous incompressible flow equations into discrete, computable algorithms [Bridson 2015]. This fertile mathematical soil has sprouted diverse numerical tools for visual simulation of drifting cigarette smoke, coiling honey, crashing ocean waves, and more [Enright et al. 2002; Fedkiw et al. 2001; Larionov et al. 2017], which are widely integrated into industrial software like *Houdini*, *Cinema4D*, and *Blender*. Yet despite the widespread use of grid-based incompressible flow animation techniques, the velocity vector fields they provide are not, in the strictest sense, incompressible!

To elucidate this potentially surprising statement, we distinguish *discrete* incompressibility from its *continuous* counterpart. Under a finite volume approach, the discrete velocity components stored

at cell face midpoints will indeed satisfy discrete incompressibility: the flux across each cell's boundary sums to zero. However, interpolation is often required to provide *pointwise* velocity values everywhere in the simulation domain, in order to support popular Lagrangian and semi-Lagrangian discretizations of advection for density, velocity, temperature, passive tracer particles, and so on [Jiang et al. 2015; Stam 1999; Zhu and Bridson 2005]. Applying basic polynomial interpolants to discretely incompressible grid data affords no guarantee that the interpolated velocity fields will be *pointwise analytically incompressible*, and in practice they are not.

Spurious compressibility has non-negligible implications. Advecting particles through vector fields with artificial sources and sinks damages volume conservation and causes uniformly distributed particles to clump and spread. Alternatively, reducing discretization error by significantly increasing grid resolution fails to address the root cause and is too costly regardless: simulation time scales cubically or worse with grid resolution. Irregular solid boundaries further exacerbate the issue because standard grid-based interpolants are essentially oblivious to obstacles; obstacle-aware cut-cell interpolants [Azevedo et al. 2016] improve enforcement of the no-normal-flow condition at the cost of worsening compression artifacts.

We therefore propose a new velocity interpolation approach, which we call the *Curl-Flow* method, that guarantees an analytically divergence-free interpolated velocity field by construction. As the name implies, we construct the velocity field \mathbf{u} by taking the curl ($\nabla \times$) of a second vector field, $\boldsymbol{\psi}$, known as a *vector potential*:

$$\mathbf{u} = \nabla \times \boldsymbol{\psi}. \quad (1)$$

Incompressibility is thus enforced by a basic vector calculus identity,

$$\nabla \cdot \mathbf{u} = \nabla \cdot \nabla \times \boldsymbol{\psi} = 0. \quad (2)$$

Our method exploits this relationship in both the discrete and continuous settings to ensure pointwise incompressibility through three steps:

- (1) Given discretely incompressible velocity values generated by a staggered grid pressure projection, construct a set of corresponding discrete vector potential values.
- (2) Interpolate the discrete vector potential values to yield a pointwise vector potential field.
- (3) Apply the continuous curl operator to the interpolated vector potential field to yield a final pointwise incompressible velocity field.

This sequence provides the conceptual framework for our method, which we flesh out in both the two- and three-dimensional settings. Making this approach practical for animation entails overcoming several theoretical and algorithmic challenges including enforcing exact zero normal velocities on exterior domain boundaries (if desired), efficiently recovering a consistent discrete vector potential, addressing null spaces in the 3D vector potential to ensure continuity and smoothness, and supporting irregular solid boundaries through cut-cells and appropriately modified interpolants.

Our novel vector potential-based divergence-free interpolation framework for staggered grid fluid animation includes the following specific technical contributions:

- An efficient parallel sweeping algorithm to recover velocity-consistent discrete vector potentials on uniform and level set-based cut-cell grids;
- A strategy to make our initial discrete 3D vector potential well-suited to interpolation (i.e., boundary-satisfying and smooth) via gauge correction with a single scalar Poisson solve;
- An additive ramping strategy for improved free-slip boundaries in the "Curl-Noise" method of Bridson et al. [2007].
- Application of this ramping method during interpolation to enforce divergence-free, *exact* no-normal-flow conditions on axis-aligned exterior domain boundaries in 2D and 3D and irregular (cut-cell) solids in 2D;
- A very simple velocity-ramping strategy to improve boundary enforcement in 3D, at the cost of introducing divergence near solids.

2 RELATED WORK

2.1 Within Computer Graphics

Various vector potential-based Eulerian approaches have previously appeared in the fluid animation literature, but most of these methods operate in the discrete realm and require solving a vector Poisson equation. Elcott et al. [2007] make use of (1) within a simplicial discretization of the vorticity equation, while Ando et al. [2015] develop a vector Poisson-based alternative to the familiar pressure projection. By contrast, our interpolation method *assumes* a discretely incompressible field as input, and recovers a corresponding discrete vector potential without a vector Poisson solve. We also use both the discrete and continuous forms together to address interpolation for advection. Notably, Ando et al. [2015] suggested the possibility of employing vector potential interpolation as future work, but did not pursue it.

Discrete vector field decomposition techniques have long been considered in graphics [Tong et al. 2003]; more recently five-component discrete decompositions were considered by Poelke and Polthier [2016] for piecewise constant vector fields on 3D triangulated surfaces and by Zhao et al. [2019] for face and edge-based tetrahedral discrete vector fields. The latter two methods also consider various choices of gauge and boundary conditions. In the context of 2D streamline recovery for flow visualization, Biswas et al. [2016] used a similar axis-based sweeping approach to ours, within a set of blocks; our approach extends this idea to irregular boundaries and to three dimensions. Similar to Ando's work, Sato et al. [2015] solved a vector Poisson problem to find the vector potential matching a discrete vector field. However, they applied the vector potential to fluid control: by deforming the underlying fluid grid carrying the potential, the flow field is deformed in a divergence-free manner. It is not clear how interpolation is performed in their scheme.

A range of procedural techniques have used pointwise divergence-free velocity fields. Stam and Fiume [1993] were the first to explore this question for gaseous phenomena, with a method that treats incompressibility by restricting cross-spectral density functions in the Fourier domain. The Curl-Noise method [Bridson et al. 2007] uses a continuous vector potential in the procedural design of animated divergence-free vector fields, while the Divergence-Free

Noise scheme of DeWolf [2006] instead uses the cross-product of two gradient fields. Divergence-free sub-grid turbulence models subsequently built on these ideas [Kim et al. 2008; Schechter and Bridson 2008]. Incidentally, Schechter and Bridson [2008] also used (but did not present or describe) a divergence-free hybrid constant-linear velocity interpolant (see their supplemental videos at time 2:18-2:27, left), which we show can be derived from bilinear stream function interpolation. This is the only prior instance of divergence-free grid-based interpolation in computer animation of which we are aware. Pointwise divergence-free vector fields have also been used in geometry processing for volume-preserving modeling [Von Funck et al. 2006] and shape interpolation [Eisenberger et al. 2018].

Like our work, Lagrangian vorticity-based simulation methods also employ a secondary vector variable to construct analytically divergence-free velocity fields; specifically, velocity is computed from vorticity via the Biot-Savart law. These methods come in many forms, including Lagrangian particles [Park and Kim 2005], filaments [Angelidis and Neyret 2005], sheets [Brochu et al. 2012; Pfaff et al. 2012], and bubbles [Da et al. 2015]. Closely related boundary integral (surface-only) methods can also offer divergence-free fields by construction [Da et al. 2016]. Model-reduced fluid simulation methods that use Laplacian eigenfunctions can offer pointwise divergence-free fields using analytical basis functions [Cui et al. 2018; De Witt et al. 2012], albeit in restricted domains (e.g., boxes).

A wide array of fundamental improvements to advection have been proposed to go beyond basic (trilinear) interpolation and (semi-Lagrangian) advection schemes [Stam 1999], ranging from the monotonic cubic interpolation of Fedkiw et al. [2001], to the MacCormack advection of Selle et al. [2008], to the "FLIP" [Zhu and Bridson 2005] and "APIC" [Jiang et al. 2015] variants of particle-in-cell schemes. Such methods tend to focus on vorticity-preservation, higher order accuracy, or diffusion-reduction. Because they ignore the fluid's divergence, we consider these approaches to be largely orthogonal, and potentially complementary, to ours.

2.2 Beyond Computer Graphics

In applied mathematics, a range of discontinuous Galerkin (DG) finite element schemes have been developed to offer pointwise divergence-free fields, often by adopting specialized incompressible basis functions on each element (e.g., [Cockburn et al. 2004; Lehrenfeld and Schöberl 2016; Rhebergen and Wells 2018]). However, DG methods tend to have a more complex implementation and do not naturally integrate with standard approaches in fluid animation; moreover, they possess pervasive field discontinuities by their very nature, which can be problematic for visual applications. In isogeometric analysis, Evans and Hughes [2013] developed exactly divergence-free Navier-Stokes simulation framework based on geometrically mapped rectangular B-spline grids; such approaches require complex mesh construction for non-trivial domains, in contrast to the simpler and more efficient cut-cell techniques often preferred in animation. In fact, these approaches replace the entire Navier-Stokes simulator, while ours provides a convenient plug-in upgrade to the advection phase of effects industry-standard methods.

In a computational fluid dynamics context, Jenny and colleagues [Jenny et al. 2001; Meyer and Jenny 2004] derived specialized 2D divergence-free node-based velocity interpolants for uniform grids and demonstrated that these offer improved particle distributions in particle-in-cell schemes. In geodynamics, Wang et al. [2015] developed the 3D extension, and Pusok et al. [2017] adapted it to face-based data by first averaging to the nodes. These approaches augment multilinear interpolants with correction terms that upgrade them to satisfy pointwise incompressibility. In an astrophysical (magnetohydrodynamics) setting, Balsara [2001, 2004] proposed divergence-free vector field reconstruction strategies based on local piecewise quadratic fitting on each cell or tetrahedron. In this strategy, one presupposes a polynomial basis and uses the divergence-free condition to determine constraints on it. Nearby vector field values or derivatives are used to solve for the coefficients. Balsara [2009] later presented an extension of this approach to Cartesian grid WENO schemes. These approaches do not consider cut-cell geometries.

Overall, in contrast to specially designed direct velocity interpolants such as those above, our choice to recover and exploit an explicit vector potential makes it comparatively easy to derive significant generalizations to higher order accuracy, global continuity/smoothness, and polyhedral cut-cell geometries, using any existing *standard* interpolation techniques, including spline interpolants and mesh-free methods.

An alternative divergence-free interpolation strategy for mesh-free point data is provided by McNally [2011], who exploits matrix-valued radial basis functions and properties of the vector Laplacian. This mesh-free method can be relatively effective, but it struggles near boundaries and we found it to be quite costly, since it requires a global solve to determine coefficients for the basis functions.

2.2.1 Vector Potentials and Gauge Conditions. The methods most similar to our own are those that work directly with vector potentials. Since a vector potential for a given velocity field is not unique, various gauge conditions are used to select a particular potential from this null space. This provides one dimension with which to categorize the schemes below. Another is whether they apply a local approach to find the vector potential, based on cell-by-cell relationships traversed in a (possibly branching) sequence, or apply a simultaneous global solution method with a linear system. We straddle these categories: our parallel sweeping approach is a cell-by-cell scheme that yields an initial potential, which we correct with a comparatively inexpensive global scalar Poisson solve to ensure smoothness. Beyond our innovations in the uniform settings in two and three dimensions, our work is particularly unique in considering interior solid geometry via cut-cells.

The implied gauge condition used in our 3D parallel sweeping method is conceptually similar to that of Ravu et al. [2016], who sought to directly construct cubic spline-based vector potentials. Like us, they begin by setting the ψ_z component to zero. However, their overall approach differs from ours in that (a) their velocity and vector potential degrees of freedom are colocated at nodes, (b) they directly seek the coefficients of continuous spline functions rather than edge-based vector potential values, and (c) they solve an expensive (compared to our parallel sweeping) global system

of equations to find the many required coefficients. Another very common gauge is the Coulomb condition, $\nabla \cdot \psi = 0$, which picks out a unique smooth vector potential and has also been used in graphics, for example, by Ando et al. [2015].

Yet another gauge condition falls out from the tree-cotree condition, explored for edge-based finite element methods by Albanese and Rubinacci [1990] on grids and Manges and Cendes [1995] on meshes. This global approach determines a spanning tree of an edge-based grid or mesh which one can assign to zero, in order to explicitly eliminate the null space of a discrete curl operator. This idea has natural connections to the traversal patterns of cell-by-cell approaches.

Bao et al. [2017] proposed a divergence-free interpolation strategy on staggered grid that reconstructs a discrete vector potential field from velocities, to improve interpolation and reduce volume conservation errors in Peskin's classic immersed boundary method [Peskin 2002] (note that Peskin's scheme uses smeared delta functions for approximate coupling with solids, rather than the sharp cut-cell approach we advocate). However, they solve for the vector potential with the Coulomb gauge, using an expensive global vector Poisson system, similar to methods used in graphics [Ando et al. 2015; Tong et al. 2003]; they also assume periodic boundary conditions which are impractical for many graphics applications.

The work of Silberman et al. [2019] in electromagnetics adopts a staggered uniform grid configuration and seeks a discrete edge-based vector potential, with the primary aim of interconverting between electromagnetics solvers based on a vector potentials \mathbf{A} magnetic fields $\mathbf{B} = \nabla \times \mathbf{A}$. They propose a local reconstruction strategy that is less parallel and more complex than ours, as it involves several special cases. Like us, they use a Poisson-based gauge transformation to enforce the Coulomb gauge, but their simpler boundary conditions enable a Fourier-based solution.

3 PROBLEM SETTING

Our method integrates into a standard grid-based fluid solver for the incompressible Euler equations that uses operator splitting [Bridson 2015; Stam 1999]. We adopt a node-based level set representation for solid objects, which leads to simple marching squares/cubes cut-cells. For cut-cell pressure projection, we use the staggered, weighted Poisson stencil approach of Batty et al. [2007] with face-area (finite volume) weights [Ng et al. 2009]. For velocity (self-)advection, we use a basic semi-Lagrangian approach for simplicity. We trace particle trajectories using third order Runge Kutta.

We develop a new velocity interpolant for use during advection,

$$\frac{\partial q}{\partial t} + \mathbf{u} \cdot \nabla q = 0, \quad (3)$$

where \mathbf{u} is the velocity field (assumed to be incompressible) and q is any scalar (e.g., density) or vector (e.g., velocity) quantity to be advected. Common advection discretizations use semi-Lagrangian [Stam 1999] or Lagrangian [Zhu and Bridson 2005] methods that trace trajectories through the flow and require interpolation to query velocity at arbitrary spatial positions. We focus on advecting passive particles, rather than velocity or other variables affecting the dynamics; this lets us use identical simulated discrete velocity fields in comparisons, isolating the effects of incompressible interpolation.

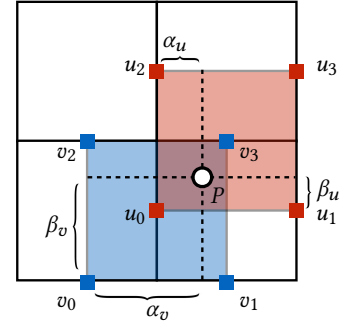


Fig. 2. **Direct Velocity Interpolation:** To compute a pointwise velocity at point $P = (x, y)$ in a staggered velocity grid, one (bilinearly) interpolates the nearby velocity samples component by component.

The simulation loop is always ordered such that advection immediately follow pressure projection [Bridson 2015], ensuring \mathbf{u} is (discretely) divergence-free. Discrete velocity component samples are placed at midpoints of cell edges in 2D (Figure 2) and centers of cell faces in 3D, so the discrete divergence-free condition is

$$\sum_{\text{faces } f} A_f u_f = 0, \quad (4)$$

where A_f is face area, and u_f is the face's outward oriented normal velocity component. (This also holds for cut-cells.)

To see the problem with standard interpolants, define a linear interpolation function $\text{lerp}(a, b, t) = (1 - t)a + tb$ and construct the bilinearly interpolated velocity at a point $P = (x, y)$ (see Figure 2) as

$$\begin{aligned} u(x, y) &= \text{lerp}(\text{lerp}(u_0, u_1, \alpha_u(x)), \text{lerp}(u_2, u_3, \alpha_u(x)), \beta_u(y)) \\ v(x, y) &= \text{lerp}(\text{lerp}(v_0, v_1, \alpha_v(x)), \text{lerp}(v_2, v_3, \alpha_v(x)), \beta_v(y)) \end{aligned} \quad (5)$$

where the α and β functions return edge fractions ($0 \leq \alpha, \beta \leq 1$) for the data indicated by their subscripts. This interpolated velocity is not analytically divergence-free in general:

$$\begin{aligned} \nabla \cdot \mathbf{u} &= \frac{\text{lerp}(u_1 - u_0, u_3 - u_2, \beta_u(y)) + \text{lerp}(v_2 - v_0, v_3 - v_1, \alpha_v(x))}{h} \\ &\neq 0 \end{aligned} \quad (6)$$

The grid cell width h appears due to the derivatives of α and β .

The left column in Figure 3 visualizes this piecewise bilinearly interpolated velocity field and its pointwise divergence for some arbitrary discretely divergence-free data on a 3×3 grid. The red box highlights a spurious sink. Advecting uniformly sampled particles through this field (Figure 4, top row), the sink region absorbs a large number of particles while other particles cluster into large and small rings (Bridson et al. [2007] call these "gutters").

While this example used staggered data, standard interpolants on node-based velocity data exhibit the same issues, since they also provide no incompressibility guarantees. Likewise, higher order polynomial interpolants do not improve divergence error or particle distributions (Figure 4, middle row). Throughout, we use the staggered bilinear (trilinear in 3D) interpolation as our baseline

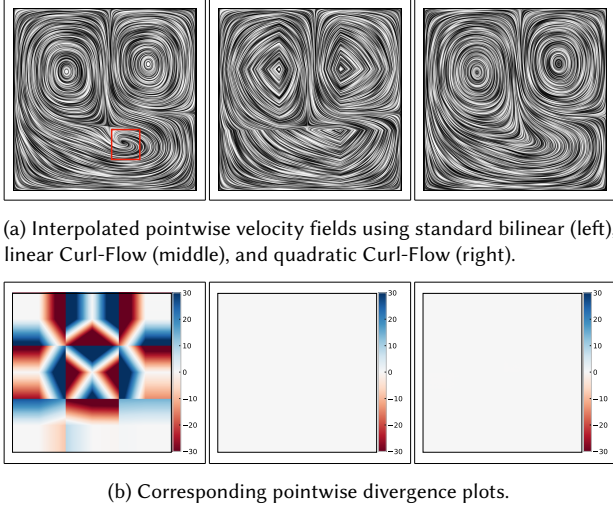


Fig. 3. **Comparison of Pointwise Divergence Between Direct Velocity Interpolation and Our Curl-Flow.** Left: A velocity field formed by bilinearly interpolating discretely divergence free velocity data on a small 3×3 grid. The red box in (a) highlights a spurious sink. Middle: A velocity field obtained using *linear* Curl-Flow interpolation. Kinks are visible in (a) due to piecewise constant velocity components, but it is nevertheless divergence free as shown in (b). Right: A velocity field with *quadratic* Curl-Flow interpolation yields a smoother flow, while remaining divergence free.

point of comparison for direct velocity interpolation, unless stated otherwise.

The middle and right column in Figure 3 show pointwise velocity fields and the corresponding pointwise divergence obtained using our approach with linear and quadratic interpolation, respectively. We use quadratic Curl-Flow interpolation in the rest of the paper to avoid velocity kinks in linear interpolation (Figure 3a, middle column), but they both contain no sinks or sources and their pointwise divergence is exactly zero.

4 CURL-FLOW INTERPOLATION IN 2D

We begin by illustrating the core principles of our approach in two dimensions. Velocity \mathbf{u} has two components, u and v , and the vector potential has one scalar component, ψ_z , called the *stream function* and denoted by non-bolded ψ . The relationship (1) simplifies to

$$u = \frac{\partial \psi}{\partial y}, \quad v = -\frac{\partial \psi}{\partial x}. \quad (7)$$

That is, \mathbf{u} is a 90° rotation of $\nabla \psi$, denoted $\nabla \psi^\perp$. To discretize, we place ψ samples at cell vertices (Figure 5) and assume ψ values vary linearly along edges. Figure 5(c) diagrams the connection between the two incident nodal ψ values and the normal component of velocity, v_n , on an edge e_{ij} having unit tangent \mathbf{e}_{ij} and length l . If we use the gradient theorem

$$\int_{e_{ij}} \nabla \psi(\mathbf{r}) \cdot d\mathbf{r} = \psi(\mathbf{x}_j) - \psi(\mathbf{x}_i) \quad (8)$$

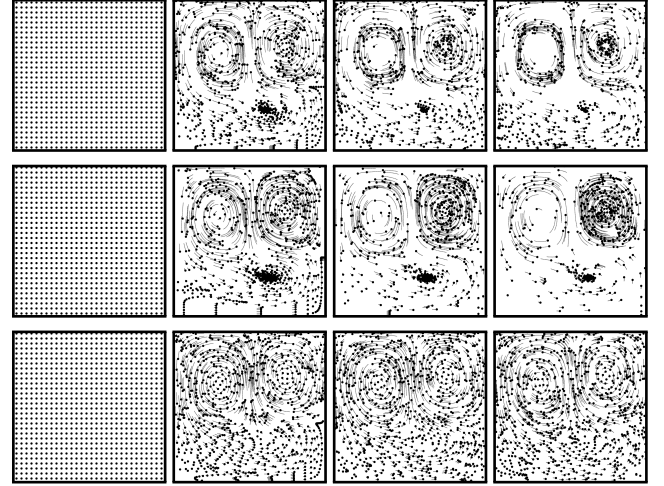


Fig. 4. **Effect on Particle Distribution:** Initially uniform particles advected through a static 2D vector field on a 3×3 grid. Frames 1, 100, 200, and 300 are shown from left to right. Top row: With direct bilinear velocity interpolation, particles become heavily clustered leaving large empty voids in the flow. Middle row: With higher order direct velocity interpolation (monotonic cubic [Fedkiw et al. 2001; Fritsch and Carlson 1980]), clustering and spreading remain significant. Bottom row: With our Curl-Flow interpolation using a quadratic kernel, particles remain much more uniformly distributed, as expected.

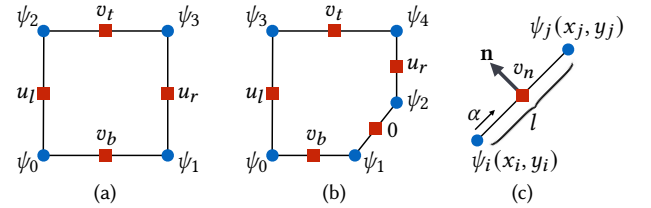


Fig. 5. **Discretization in 2D:** Locations of discrete velocity samples (red squares) and discrete stream function samples (blue circles). (a) grid cell. (b) cut-cell clipped by a static solid object. (c) relationship between edge normal velocity and stream function samples. For this case, $v_n = -(\psi_j - \psi_i)/l$.

and discretize it on each edge, we get

$$\frac{\psi_j - \psi_i}{l} = \nabla \psi \cdot \mathbf{e}_{ij} = \nabla \psi^\perp \cdot \mathbf{e}_{ij}^\perp = v_n (\mathbf{n} \cdot \mathbf{e}_{ij}^\perp). \quad (9)$$

Since \mathbf{e}_{ij}^\perp is oriented and always matches \mathbf{n} up to a sign flip, the dot product simply determines the sign.

4.1 Uniform Grids in 2D

4.1.1 Recovering discrete ψ . For a single uniform grid cell as in Figure 5(a), (9) leads to

$$\begin{aligned} u_l &= \frac{\psi_2 - \psi_0}{h}, & u_r &= \frac{\psi_3 - \psi_1}{h}, \\ v_b &= -\frac{\psi_1 - \psi_0}{h}, & v_t &= -\frac{\psi_3 - \psi_2}{h}, \end{aligned} \quad (10)$$

consistent with finite differences on (7). Given the velocities, we would like to find the ψ_i . These equations possess a one-dimensional

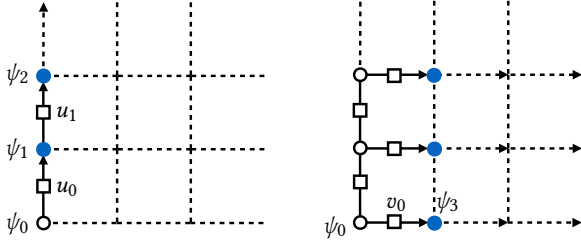
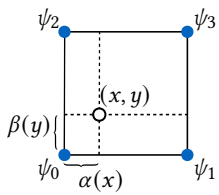


Fig. 6. **Parallel Sweeping** efficiently recovers a 2D uniform grid discrete stream function field. Left: First, sequentially compute all ψ values at $x = x_0$, starting from $\psi_0 = 0$ and sweeping in the y direction. Right: Next, compute the remaining ψ values by sweeping in the x direction in parallel.

null space: constant offsets of all ψ_i do not change the velocities. Physically, the divergence-free condition ensures one of the fluxes is the negated sum of the others, implying one equation is linearly dependent. We select a unique solution by arbitrarily setting $\psi_0 = 0$. We can then determine the other ψ_i by linear-time back-substitution; this is equivalent to traversing the cell's edge graph, computing each subsequent ψ value from its predecessor on the edge and the edge's velocity component. The divergence-free condition ensures discrete integrability, i.e., looping back to ψ_0 gives a consistent result.

Applying the relationships of (10) to an entire uniform grid yields a large sparse system of equations, yet the same graph traversal strategy remains effective. This avoids a traditional (and costly) global Poisson solve for ψ based on (2). Any traversal order through the grid's edges suffices, but an order that maximizes parallelism is preferable. As in Figure 6, we first set $\psi_0 = 0$, and sweep vertically to obtain all the ψ values at $x = x_0$ (i.e., $\psi_1 = \psi_0 + hu_0$ and so on). We then sweep in the horizontal direction in parallel to obtain all remaining ψ values. This approach will also recover correct values in the presence of boundaries with prescribed velocities, such as the inflow/outflow boundaries in several of our examples. In the absence of solid obstacles, the sweeping method is consistent with that of Biswas et al. [2016].



4.1.2 Interpolating ψ . Interpolation of the grid ψ values provides an analytical stream function at any point. Applying the curl operator $(\frac{\partial}{\partial y}, -\frac{\partial}{\partial x})$ to the interpolant we obtain a velocity field which is *pointwise* divergence-free by construction. For example, simple bilinear interpolation yields

$$\begin{aligned}\psi(x, y) &= \text{lerp}(\text{lerp}(\psi_0, \psi_2, \beta(y)), \text{lerp}(\psi_1, \psi_3, \beta(y)), \alpha(x)), \\ u(x, y) &= \frac{\text{lerp}(\psi_2 - \psi_0, \psi_3 - \psi_1, \alpha(x))}{h} = \text{lerp}(u_l, u_r, \alpha(x)), \\ v(x, y) &= -\frac{\text{lerp}(\psi_1 - \psi_0, \psi_3 - \psi_2, \beta(y))}{h} = \text{lerp}(v_b, v_t, \beta(y)),\end{aligned}$$

where the rightmost equivalences follow from (10). The analytical divergence of this velocity is zero,

$$\nabla \cdot \mathbf{u} = \frac{u_r - u_l + v_t - v_b}{h} = 0, \quad (11)$$

which follows from the discrete divergence being zero. However, this field is piecewise constant in one axis and piecewise linear in the other, which introduces tangential discontinuities between cells.

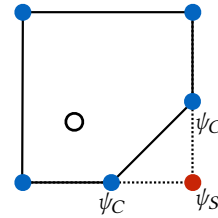
Fortunately, our choice to work with the stream function means we can recover velocity continuity simply by upgrading the interpolant applied to ψ to a higher polynomial degree. Although many choices are possible, we adopt the quadratic dyadic B-spline kernels popular in material point methods [Jiang et al. 2016; Steffen et al. 2008]; they are sufficiently smooth and possess relatively small stencils for efficiency. It is also straightforward to take their curl analytically. Interestingly, the simple uniform grid bilinear case above boiled down to an interpolant that sidesteps ψ altogether, requiring only discrete u, v . However, deriving such direct incompressible velocity interpolants becomes nontrivial in general; again relying on ψ enables us to extend our method far more easily to irregular polygonal cut-cell geometry, while also preserving the smoothness of quadratic (or higher order) interpolants.

4.2 Cut-Cells in 2D

4.2.1 Recovering discrete ψ . Considering cut-cell solids during stream function reconstruction process only requires accounting for truncated grid edges and non-axis-aligned "cut edges". Applying (9) we get an update rule for sweeping through such edges:

$$\psi_{i+1} = \psi_i + l_{i,i+1} v_{i,i+1} (\mathbf{e}_{i,i+1}^\perp \cdot \mathbf{n}_{i,i+1}). \quad (12)$$

We restrict our focus to stationary solid obstacles for which the surface normal component of velocity is zero. This implies that the recovered ψ will be constant on the surface, i.e., an isocontour along which particles should slide in a free-slip manner. The stationary assumption also preserves the simplicity of parallel sweeping; nodal stream function values at the entry and the exit point of a grid line through a solid obstacle are identical.



4.2.2 Interpolating ψ . With cut-cell solids, the nodal ψ values (blue in the inset) no longer fall on a perfect uniformly spaced grid. One could use the mesh-free moving least squares (MLS) interpolation based on ψ data in a neighborhood. However, it requires solving small dense linear systems which becomes expensive and computing its analytical derivatives

is known to be non-trivial [Huerta et al. 2004]. Instead we extrapolate ψ values to uniform grid nodes inside the solid (i.e., ψ_S in the inset) and use quadratic B-spline kernels as in the uniform grid case. This extrapolation can be done in various ways, such as using MLS or simply copying (e.g., from ψ_C to ψ_S) assuming discrete flux is zero on interior solid edges (dashed lines); we adopt the latter for simplicity. At the outer axis-aligned domain boundaries, the quadratic stencil is likewise missing data samples, so we add an additional uniform layer of ψ samples outside the domain and fill it by extrapolation (copying). However, regardless of these extrapolation and interpolation choices near boundaries, the no-normal-flow condition is enforced only approximately; we propose an additional correction below.

4.2.3 A Curl-Noise enhancement for exact 2D boundary enforcement.

To ensure that the interpolated ψ will be *strictly* constant along the polygonal boundary, we adapt ideas from the Curl-Noise method [Bridson et al. 2007]. That method modulates the existing ψ value near obstacles, forcing it to zero on the boundary by multiplying against a smooth ramp function based on boundary proximity. Defining d_0 as an influence radius (we use h), $d(\cdot)$ as the distance to the surface, and $\text{ramp}(\cdot)$ as Bridson's ramp function, the multiplicative factor is $\alpha = \text{ramp}(d(\mathbf{x})/d_0)$, giving a correction of $\psi'(\mathbf{x}) = \alpha\psi(\mathbf{x})$.

In general however, the desired constant boundary ψ_c (known at the solid nodes) is often *not* zero, leading to dramatic spurious flow deviations (Figure 7). We therefore modified Bridson's method by also ramping the target value on:

$$\psi'x = \alpha\psi(\mathbf{x}) + (1 - \alpha)\psi_c \quad (13)$$

However, the initial multiplication still appreciably damages the *normal derivatives* of ψ . Since $\mathbf{u} = \nabla \times \psi$ implies $\mathbf{u} \cdot \mathbf{t} = \frac{\partial \psi}{\partial \mathbf{n}}$, where \mathbf{t} is the boundary tangent vector, this induces undesired tangential damping, acceleration, or no-slip behavior (Figure 8, bottom).

We propose a new purely *additive* ramping procedure that instead enforces ψ_c by computing and adding a compensating offset. The required offset is determined by interpolating ψ at the closest boundary point and subtracting it from ψ_c . Letting $cp(\cdot)$ be a function that returns the closest boundary point, we modify ψ as:

$$\psi'(\mathbf{x}) = \psi(\mathbf{x}) + (\psi_c - \psi(cp(\mathbf{x}))) (1 - \alpha). \quad (14)$$

This expression ramps the full additive correction precisely on at the boundary ($d(\mathbf{x})/d_0 = 0$) and blends it smoothly off at the edge of the influence region ($d(\mathbf{x})/d_0 = 1$). The inset shows an example input ψ curve (black), and the result after using multiplicative (red) and our additive (green) ramping to $\psi_c = 0$. Both methods correct the value, but additive ramping better preserves the derivative near the boundary and thus yields more faithful free-slip flow (Figure 8, top). (At prescribed nonzero inflow/outflow boundaries or open boundaries, we do not apply ramping.) When querying velocity, as we did for the interpolation kernels, we use the analytical curl to determine this added contribution.

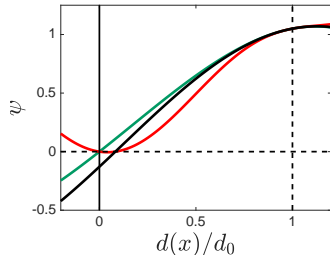


Figure 9 shows a comparison of direct (bilinear) velocity interpolation vs. our complete Curl-Flow method (including additive ramping boundary correction) on a steady-state flow past a disk. For direct velocity interpolation in the presence of irregular objects, we extrapolate fluid velocities to grid samples inside the solid [Houston et al. 2003; Rasmussen et al. 2004] to approximate free-slip behavior.

5 CURL-FLOW INTERPOLATION IN 3D

Moving to three dimensions introduces new challenges. The scalar stream function ψ is replaced by the vector potential $\boldsymbol{\psi} = (\psi_x, \psi_y, \psi_z)$, and thus each velocity component is dictated by the *interactions* of two ψ components' derivatives (e.g., $u = \partial\psi_z/\partial y - \partial\psi_y/\partial z$). This

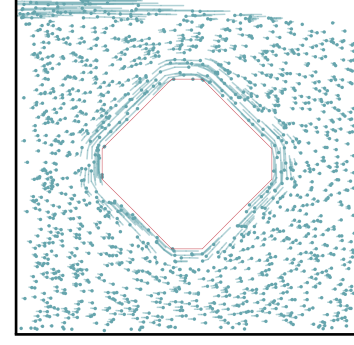


Fig. 7. **Boundary Ramping Issues:** A steady left-to-right flow with a naive ramping-based "correction" at the top, bottom, and internal solid boundaries. Because the true discrete ψ_c value differs at each surface, Bridson's multiplicative ramping to $\psi_c = 0$ causes spurious tangential flow near the obstacle, undesired no-slip at the bottom where ψ is already zero, and large reverse flow at the top.

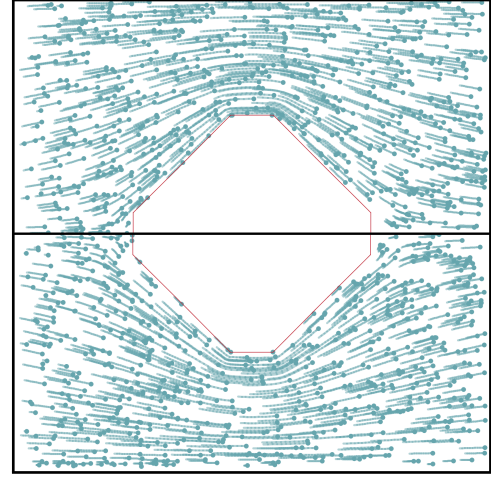


Fig. 8. **Additive vs. Multiplicative Ramping:** A steady left-to-right flow (faster than in Figure 7) with boundary ψ_c value adjustment. Top half: Our additive ramping exactly satisfies the boundary with no apparent damping of free-slip tangential velocities. Bottom half: Despite modifying Bridson's multiplicative ramp to properly target the desired ψ_c , tangential damping at the bottom and near the solid occurs, since it damages $\partial\psi/\partial\mathbf{n}$.

interaction complicates boundary enforcement, especially for irregular geometry. The curl operator also possesses a multi-dimensional null space, necessitating enforcement of a *gauge condition* to find an appropriate unique $\boldsymbol{\psi}$.

5.1 Uniform Grids in 3D

As shown in Figure 10, we place vector potential components on cell edges and velocity normal components on cell faces [Ando et al. 2015; Elcott et al. 2007]. Given discretely divergence-free face velocities from the pressure projection step, we seek corresponding edge vector potential values for subsequent interpolation.

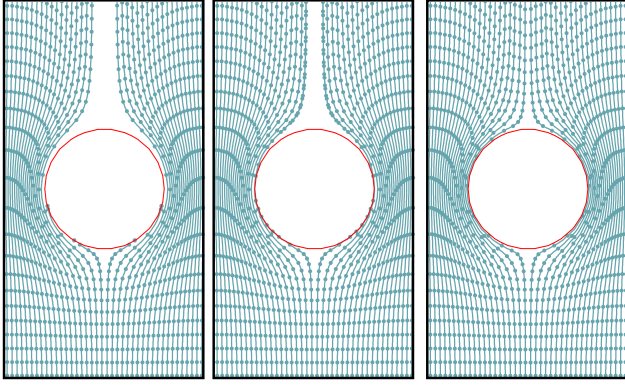


Fig. 9. **Flow Near Solids:** Particle trajectories flowing from bottom to top under a fixed (steady state) flow past a red solid disk in 2D. Grid resolution: 30×15 . Left: Direct velocity interpolation induces spurious trailing gaps, when trajectories colliding with the solid are terminated. Middle: With the same velocity interpolant, projecting penetrating particles back to the surface does not significantly improve divergent trajectories to “close up” and unwanted particle clumping occurs. Right: Our Curl-Flow method better respects solid boundaries and produces less spurious empty space behind the solid. Notice the trajectories are simply isocontours of the 2D ψ field.

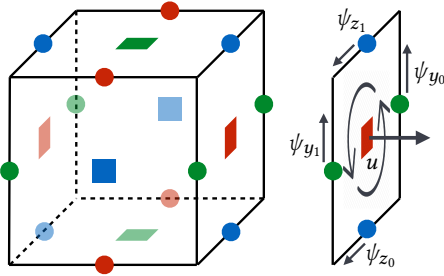


Fig. 10. **Discretization in 3D:** Discrete vector potential samples are located on cell edges (circles) and velocity samples are on cell faces (squares). Red, green, and blue represent x , y , and z components of ψ , respectively.

We assume that the input axis-aligned exterior domain boundaries have zero normal velocity. For a boundary u -face, this implies $\frac{\partial \psi_z}{\partial y} - \frac{\partial \psi_y}{\partial z} = 0$, i.e., the sum of these tangential derivatives is zero. As noted by Bridson et al. [2007], a simple way to achieve this is setting both tangential components of ψ to a constant value of zero. Thus, the continuous problem we are solving is

$$\begin{aligned} \nabla \times \psi &= \mathbf{u} & \text{in } \Omega, \\ \psi &= 0 & \text{on } \partial\Omega. \end{aligned} \quad (15)$$

To discretize, consider that the flux across a surface, in terms of the vector potential, is

$$\iint_S \mathbf{u} \cdot d\mathbf{S} = \iint_S (\nabla \times \psi) \cdot d\mathbf{S} = \int_C \psi \cdot d\mathbf{r}, \quad (16)$$

where S is an oriented smooth surface, C is the oriented boundary curve of the surface, and \mathbf{r} is the boundary tangent direction. (The second equality holds by Stokes’ theorem.) Discretizing (16) with midpoint quadrature for the single face in Figure 10, right, we have

$$u_f h^2 = \sum_{e \in E} \psi_e \cdot (h \mathbf{e}_e) = h(\psi_{y_0} + \psi_{z_1} - \psi_{y_1} - \psi_{z_0}), \quad (17)$$

where h is a cell width and \mathbf{e}_e is the oriented unit normal vector along an edge. (Finite differencing of $\mathbf{u} = \nabla \times \psi$ would yield the same result.) Equation 17 relates four unknown edge ψ_e values to one face u_f velocity. Stacking the equations for all grid faces yields a global sparse linear system.

Solving (15) is an inverse curl problem having infinitely many solutions. For example, a single cell has a seven-dimensional null space: there are 12 edge-based ψ_e unknowns and just five linearly independent face u_f values (the sixth is made redundant by incompressibility). A unique solution can be selected by choosing a gauge condition [Silberman et al. 2019]. We adopt the popular *Coulomb* gauge, which enforces zero divergence of the vector potential ($\nabla \cdot \psi = 0$). It offers maximal smoothness of the ψ field, which will be attractive for interpolation.

Direct application of the Coulomb gauge condition leads to a vector Poisson problem for ψ ,

$$\nabla \times (\nabla \times \psi) + \nabla (\nabla \cdot \psi) = \nabla \times \mathbf{u}, \quad (18)$$

that is about three times the size and cost of a standard pressure projection (e.g., [Ando et al. 2015]). Fortunately, unlike the setting considered by Ando et al., our discrete velocities are *already* incompressible, enabling us to solve (15) much more efficiently.

Observe that

$$\mathbf{u} = \nabla \times \psi = \nabla \times (\psi + \nabla \phi) = \nabla \times \psi', \quad (19)$$

where ϕ is an arbitrary scalar field. Since $\nabla \times \nabla \phi$ is always zero (by second derivative identities of vector calculus), defining $\psi' = \psi + \nabla \phi$ gives another valid vector potential field. Leveraging this characterization of the null space, we propose a new algorithm consisting of two steps. First, find one *valid but arbitrary* vector potential field through an efficient parallel sweeping scheme (Section 5.1.1), analogous to the 2D case. Second, modify the obtained ψ field to satisfy the Coulomb gauge $\nabla \cdot \psi = 0$ and our boundary condition $\psi = 0$ using a carefully constructed ϕ (Section 5.1.2).

5.1.1 Recovering a Vector Potential by Parallel Sweeping. Our first objective is to find a velocity-consistent discrete vector potential field on a box-shaped domain, without the ψ boundary condition or gauge. Our fast 3D parallel sweeping strategy is illustrated in Figure 11.

- (1) Set $\psi_z = 0$ (or a constant) *everywhere* in the domain (Figure 11, top-left). This is safe because the remaining two components (ψ_x, ψ_y) still suffice to represent any set of three velocity components (u, v, w).
- (2) Compute velocity-satisfying vector potential values for the $z = z_{\min}$ boundary plane. Since we are considering the zero normal flux case, we simply set all ψ_x and ψ_y values to zero (Figure 11, top-right).

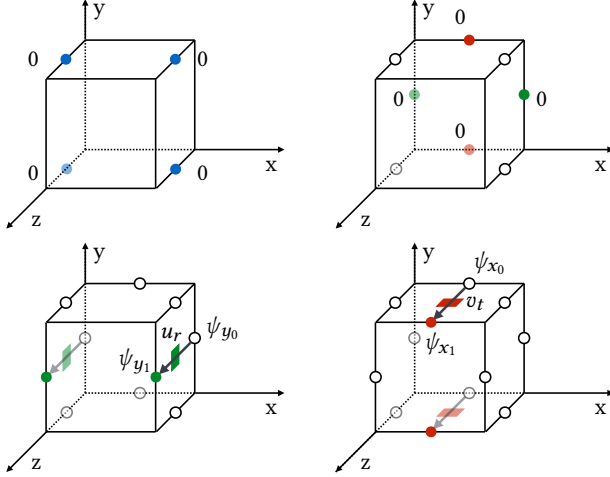


Fig. 11. **Parallel Sweeping in 3D:** Top-left: Set all ψ_z values to be zero. Top-right: Compute satisfying ψ_x and ψ_y values at $z = z_{min}$. In this example they are all set to zero. Bottom-left: Starting from ψ_y values at $z = z_{min}$, we can compute all ψ_y values in the entire domain in one sweep using the relation $\psi_{y1} = \psi_{y0} - hu_r$. Bottom-right: Starting from ψ_x values at $z = z_{min}$, we can compute all ψ_x values in the entire domain in one sweep using the relation $\psi_{x1} = \psi_{x0} + hv_t$.

- (3) Compute the remaining vector potential values by parallel sweeping. Equation 17 and $\psi_z = 0$ give $\psi_{y1} = \psi_{y0} - hu$ (Figure 11, bottom-left), and likewise $\psi_{x1} = \psi_{x0} + hv$ (Figure 11, bottom-right). In this manner, the values of ψ_{x_n} and ψ_{y_n} , along with the discrete velocities, dictate $\psi_{x_{n+1}}$ and $\psi_{y_{n+1}}$ as we sweep across the entire domain.

At the conclusion of this process the discrete velocity condition (17) is met on all grid faces, $\psi_z = 0$ everywhere, and we have zero ψ_x and ψ_y values on all the boundaries, with the important exception of the $z = z_{max}$ boundary plane. (As in 2D, our approach can be straightforwardly generalized to inflow/outflow conditions at the outer domain boundaries.) Next, we would like to modify this ψ to enforce the gauge and boundary conditions.

5.1.2 Modifying a Vector Potential via the Null Space. To satisfy the boundary condition $\psi = 0$ we construct a discrete scalar field ϕ_{BC} defined at the nodes of cells so the discrete $\nabla\phi_{BC}$ components coincide with the edge-based discrete vector potential components ψ_x , ψ_y , and ψ_z [Ando et al. 2015; Silberman et al. 2019]. Seeking a boundary condition of $\psi' = 0$ gives the problem

$$\psi + \nabla\phi_{BC} = 0 \quad \text{on } \partial\Omega. \quad (20)$$

We wish to solve for ϕ_{BC} with ψ already known from sweeping. Setting boundary conditions only requires modifying ψ edges on the domain boundary, so we only need to find nonzero ϕ_{BC} values on the boundary. Furthermore, our parallel sweeping process already ensured that the only non-zero boundary values left to be eliminated are ψ_x and ψ_y on the $z = z_{max}$ boundary plane. Therefore, finding nonzero ϕ_{BC} values only on $z = z_{max}$ suffices. Without loss of generality, we set the outer boundary loop of nodal ϕ_{BC} values on this plane (black/white diamonds in Figure 12) to zero, and compute

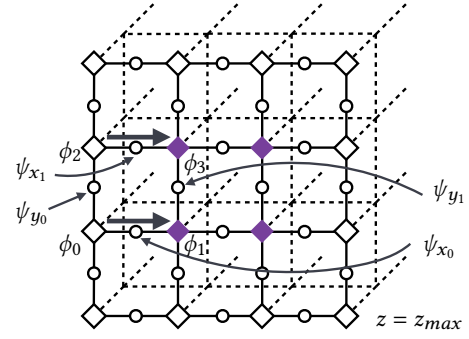


Fig. 12. **Gauge Correction Boundary Conditions:** We construct $\nabla\phi_{BC}$ to update boundary ψ components to satisfy no-normal-flow. Black/white circles, black/white diamonds, and purple diamonds represent known vector potential values, pinned ϕ values, and unknown ϕ values, respectively. Unknown ϕ values are computed from the pinned or previously computed ϕ values ($\phi_1 = \phi_0 - h\psi_{x0}$, $\phi_3 = \phi_2 - h\psi_{x1}$).

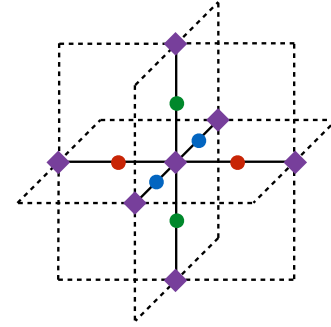


Fig. 13. **Gauge Correction:** A uniform grid scalar Poisson solve is used to find a nodal scalar field ϕ (purple diamonds). Adding $\nabla\phi$ to the vector potential values, ψ_x (red disks), ψ_y (green disks), and ψ_z (blue disks), satisfies the Coulomb gauge condition, $\nabla \cdot \psi' = \nabla \cdot (\psi + \nabla\phi) = 0$.

the remaining ϕ_{BC} values in the plane by traversing the interior edges using $\phi_{next} = \phi_{prev} - h\psi_e$; this is essentially the same process as in solving the 2D stream function problem.

If we were to add this $\nabla\phi_{BC}$ field to ψ (including any interior edges touching the nonzero ϕ values), we will have satisfied our desired boundary condition on the z_{max} boundary plane, without breaking the consistency between the discrete u and ψ . The resulting valid vector potential would possess an *implicit* gauge condition on ψ , resulting from parallel sweeping and boundary correction. Unfortunately, this gauge offers no meaningful guarantees on the presence or absence of large discontinuous jumps in the discrete vector potential. Although applying an interpolant and taking the curl will necessarily yield a pointwise divergence-free field, the observed pointwise velocity behavior can be quite irregular depending on interactions between the data jumps and the interpolant, since it is the interactions among vector potential derivatives that dictate velocity. We therefore finish recovering ψ by enforcing the Coulomb

gauge condition $\nabla \cdot \psi = 0$ on the interior, which provides a canonical and optimally smooth vector potential field for interpolation.

Defining a new global nodal ϕ field, we enforce the Coulomb gauge condition using a gauge correction similar to that of Silberman et al. [2019] (they adopt different boundary conditions). This can be written as $\nabla \cdot \psi' = \nabla \cdot (\psi + \nabla \phi) = 0$, giving a node-based scalar Poisson problem for ϕ with Dirichlet boundary conditions:

$$\begin{aligned} \nabla \cdot \nabla \phi &= -\nabla \cdot \psi & \text{in } \Omega \\ \phi &= \phi_{BC} & \text{on } \partial\Omega \end{aligned} \quad (21)$$

After solving for ϕ we update the vector potential with $\psi' = \psi + \nabla \phi$, similar to the velocity update in a classic pressure projection.

5.1.3 Interpolation. Our choice for 3D uniform grid interpolation naturally generalizes from 2D: we use quadratic dyadic B-spline kernels separately on each staggered component of ψ . (Other quadratic or higher order interpolants would also suffice.) Since we have enforced zero discrete tangential ψ components on the axis-aligned domain exterior, in this special case we can easily ensure exactly zero pointwise boundary flux by ramping each of the two tangential components to zero, in the manner described by Bridson et al. [2007], albeit substituting our improved *additive* free-slip ramp instead.

5.2 Cut-Cells in 3D

The interference of cut-cell solid objects requires that we adapt our approach to retain the use of the simple and efficient parallel sweeping method and to apply gauge correction in an approximate fashion. We then apply a modified interpolation strategy to enforce the desired boundary behavior.

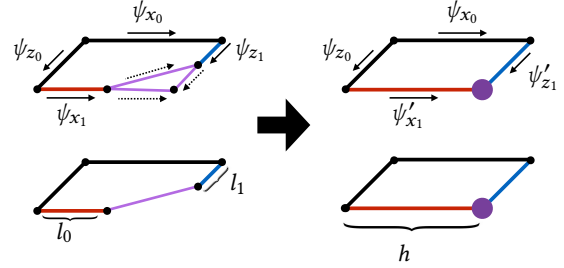
5.2.1 Parallel Sweeping with 3D Cut-Cells. Unmodified parallel sweeping proceeds face by face assuming every cell is uniform and all active edges are axis-aligned. To adapt parallel sweeping to cut-cells, we will conceptually perturb the solid geometry so that this algorithm can still proceed while recovering ψ values that preserve the correct flux even on cut-cell fluid faces.

We assume that axis-aligned edges interior to the solid region have zero vector potential on the edge, including the solid portion of partial cut edges (e.g., two of the three purple edges in Figure 14(a)). Within each axis-aligned planar partial face, we therefore collapse the solid portion of each axis-aligned cut edge onto the incident interior solid grid node, so the partial fluid edge becomes entirely fluid. This has the side effect of also collapsing away non-axis-aligned solid edges (e.g., the diagonal purple edge in Figure 14(a)), whose contributions are likewise assumed to be zero. We can then safely apply parallel sweeping as before, adjusting the relevant per-face equations to compensate for the "stretched" fluid edges.

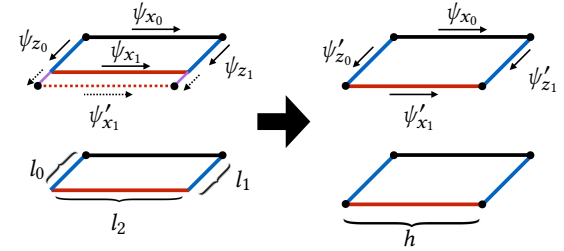
For example, since we assumed zero values for the (collapsed) purple edges, the top face in Figure 14(a) left, is discretized according to (16) as

$$v_t A W_t = h \psi_{z_0} + l_0 \psi_{x_1} - l_1 \psi_{z_1} - h \psi_{x_0} \quad (22)$$

where v_t is the velocity normal component on the top face, $A = h^2$ is the area of a regular (non-cut) cell face, the l_i are the true lengths of partial fluid edges, and W_t is the fluid area fraction of the top face. When we apply parallel sweeping on ψ_x from back to front, we can



(a) Purple triangle (top left) is collapsed to the purple point (top right) and the new ψ' values in regular cells are length fractions times the original ψ values ($\psi'_{x_1} = \frac{l_0}{h} \psi_{x_1}$, $\psi'_{z_1} = \frac{l_1}{h} \psi_{z_1}$). (Bottom row indicates edge lengths.)



(b) Two purple edges (top left) are collapsed (top right) and the ψ values are rescaled accordingly ($\psi'_{z_0} = \frac{l_0}{h} \psi_{z_0}$, $\psi'_{z_1} = \frac{l_1}{h} \psi_{z_1}$, $\psi'_{x_1} = \frac{l_2}{h} \psi_{x_1}$). (Bottom row indicates edge lengths.)

Fig. 14. **Adapting Parallel Sweeping to Cut-Cells:** Fluid cut-edges in cut-cells are converted to uniform edges by assigning zero ψ to solid purple edges and (conceptually) collapsing them; this enables uniform grid sweeping to proceed.

recover ψ_{x_1} from ψ_{x_0} using (22) since all ψ_z are set to zero in our sweeping algorithm.

This face-centric approach extends to cover all geometries of axis-aligned cut-faces (i.e., the marching squares cases), with minor modifications. In Figure 14(b), consider that the (unmodified) top face consists of a fluid part (nonzero flux) and a solid part (zero flux). These two (sub-)faces implies two equations,

$$\begin{aligned} v_t A W_t &= l_0 \psi_{z_0} + l_2 \psi_{x_1} - l_1 \psi_{z_1} - h \psi_{x_0}, \\ 0 &= l_2 \psi_{x_1} - h \psi'_{x_1}. \end{aligned} \quad (23)$$

where the second equation relies on assigning zero to the two short purple edges. Therefore, we can find ψ_{x_1} and ψ'_{x_1} via sweeping.

The second equation in (23) also highlights that the original and stretched edge ψ values are always related by a simple length rescaling: $\psi'_{x_i} = (l_i/h) \psi_{x_i}$. Our modified sweeping algorithm thus becomes even simpler: apply uniform grid parallel sweeping (§5.1.1) over the full domain, assuming zero velocity on fully interior solid faces and zero vector potential on fully interior solid edges; then simply rescale the ψ values on partially cut edges to recover their correct values.

5.2.2 Gauge Correction and Interpolation with 3D Cut-Cells. It becomes more difficult to apply gauge correction with cut-cell solids, since the discrete vector potential samples no longer lie conveniently

on uniform grid edges and the Coulomb zero-divergence condition should be enforced at nodes of the polyhedral cut-cells. Regardless, interpolating arbitrary-directional vector potential components is unwieldy and, as we saw in 2D, would still require an additional correction to better respect the solid boundary. We therefore take a simpler approximate approach: we use the "stretched" vector potentials and conceptually uniform faces determined above (Figure 14), and perform gauge correction as before on the entire uniform grid, including through the interior of solids, by assuming zero flux on interior solid faces. This provides gauge-corrected axis-aligned ψ values everywhere, which we use for quadratic B-spline kernel interpolation as in the uniform case. Finally, we improve the boundary treatment with a correction mechanism as described below.

5.2.3 Approximate Boundary Correction for 3D Cut-Cells. A typical treatment of irregular boundaries during interpolation is to extrapolate the fluid velocity into solids, and optionally (approximately) project out the solid normal velocity component at each grid sample [Houston et al. 2003; Rasmussen et al. 2004]; this is often still insufficient, since the grid-interpolant won't faithfully reflect the sub-grid surface position. As such, particles must also be very frequently projected out of solids and back into the flow, exacerbating particle clumping. Azevedo et al. [2016] used generalized barycentric coordinates on the conforming cut-cell meshes to coerce the velocity field to precisely align with boundaries, but this approach is specialized to their simulation setup.

We propose a very simple, fast, and general alternative to ensuring a vector field that enforces precise no-normal-flow at the sub-grid solid boundary, and which we have not seen presented elsewhere. We apply the same distance-based ramping procedure used earlier on the potential, but applied instead to the normal component of velocity to match the solid normal velocity as a particle approaches:

$$u'_n = u_n + (u_{solid} \cdot n - u(cp(x)) \cdot n)(1 - \alpha). \quad (24)$$

Here, we used a classic *smoothstep*(\cdot) substituted for Bridson's *ramp*(\cdot) when finding the blending parameter α ; however, both additive and (modified) multiplicative ramping with either *ramp*(\cdot) or *smoothstep*(\cdot) all gave similar results in our tests.

Applied as a "velocity filter" during interpolation, this approach will yield a velocity field *exactly* satisfying the boundary condition everywhere on the surface, but because it is based on velocity (rather than potential as in our 2D treatment) it will typically somewhat harm the divergence-free property near the solid, similar to prior approaches discussed above. However, this strategy has several benefits: it is easily applicable to essentially *any* velocity-based simulation, fast to apply, and graceful in handling modestly sub-grid geometry. We achieved visually compelling results in the scenarios on which we tested it.

6 RESULTS

To consistently compare our Curl-Flow method against direct velocity interpolation (i.e., bi/trilinear unless otherwise noted) we always use the exact same setup aside from the interpolation method. That is, we use identical discretely divergence-free velocity data generated by the same simulation for both approaches and visualize with massless tracer particles. Furthermore, only *particle advection*

differs, even for time-dependent (unsteady) flows. Velocity (self-) advection still uses semi-Lagrangian scheme [Stam 1999] with basic bi-/tri-linear velocity interpolation.

When a particle incorrectly penetrates a solid object due to either a poor velocity field or path integration errors, it is typical to "resolve" the collision by directly projecting the particle back out of the solid in the normal direction (although this exacerbates clumping). However, to better emphasize where such errors occur, when a particle reports a collision we simply freeze it in place forever (unless otherwise indicated).

6.1 2D Results

The 2D version of Curl-Flow is particularly attractive in practice because it does not require any linear solve for gauge correction, and gives perfectly conforming velocity fields with pointwise incompressibility everywhere. In the earlier 2D results of Figures ??, ??, 4, 7, 8, and 9, we used static velocity fields to illustrate the influence of velocity interpolation on (unchanging) particle trajectories. In the 2D examples that follow, we generate more realistic time-evolving velocity data with a proper simulation and observe how our approach affects the particle motion and density in this setting.

Smooth Obstacle Comparison. In Figure 15, we observe particles under a dynamic horizontal flow past a circular solid. Although we began with a completely filled domain, spurious gaps are quickly produced with direct velocity interpolation. Our Curl-Flow method better obeys the boundary and exactly satisfies incompressibility, dramatically reducing the gaps in the flow.

Jagged Obstacle Comparison. The same effect can be observed for non-smooth geometry: Figure 16 shows a test case with two W-shaped solid objects in a horizontal flow. With direct velocity interpolation, we observe significant gaps trailing the obstacle and around its high curvature features. We are able to significantly reduce these artifacts using Curl-Flow.

6.2 3D Results

To demonstrate the importance of pointwise incompressible velocity fields in 3D, Figure 1 compares our Curl-Flow method against the results of direct velocity interpolants with both (componentwise) trilinear and monotonic tricubic [Fedkiw et al. 2001; Fritsch and Carlson 1980], as these are relatively common choice in fluid animation. The data is a $5 \times 5 \times 5$ discretely incompressible staggered grid discrete vector field, where the velocity data is held constant for the length of the animation to factor out the effects of the dynamics. The direct interpolants quickly exhibit clustering and thinning out of particles, leaving visible low densities in some regions and denser ring-like patterns in others. By contrast, the Curl-Flow result remains remarkably uniformly distributed for the length of the animation, with no particle resampling, perturbation, or other remedies applied.

To examine the behavior of our 3D Curl-Flow method with cut-cells, we simulate a flow past a spherical solid object with a fixed velocity field (Figure 17), and release a planar layer of passive particles. With trilinear advection, many of the particles collide with

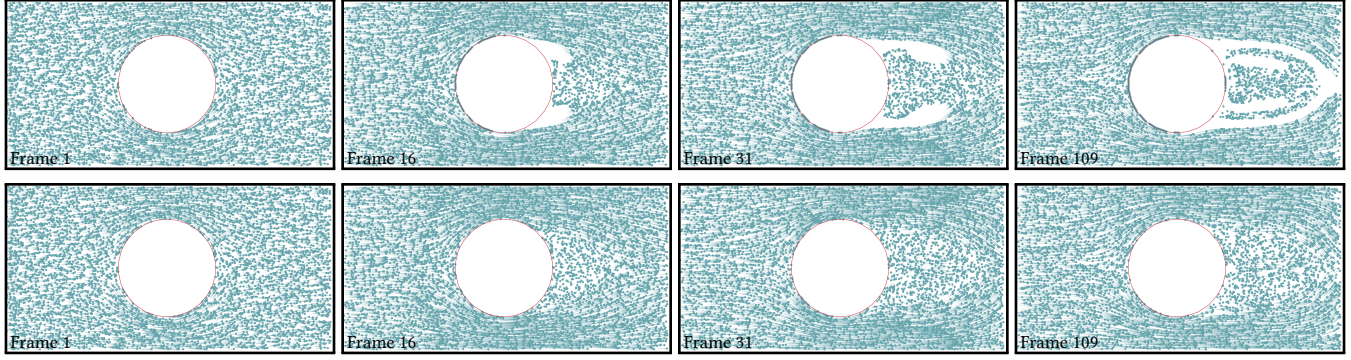


Fig. 15. **Smooth Obstacle Comparison:** Top: Particles undergoing a time-dependent horizontal flow past a circular object using bilinear direct velocity interpolation. Particles colliding with objects are halted in place for illustration. The interpolated field does not tightly follow the solid object and thus produces empty space behind it. Bottom: The same velocity field under Curl-Flow interpolation significantly reduces gaps in the flow.

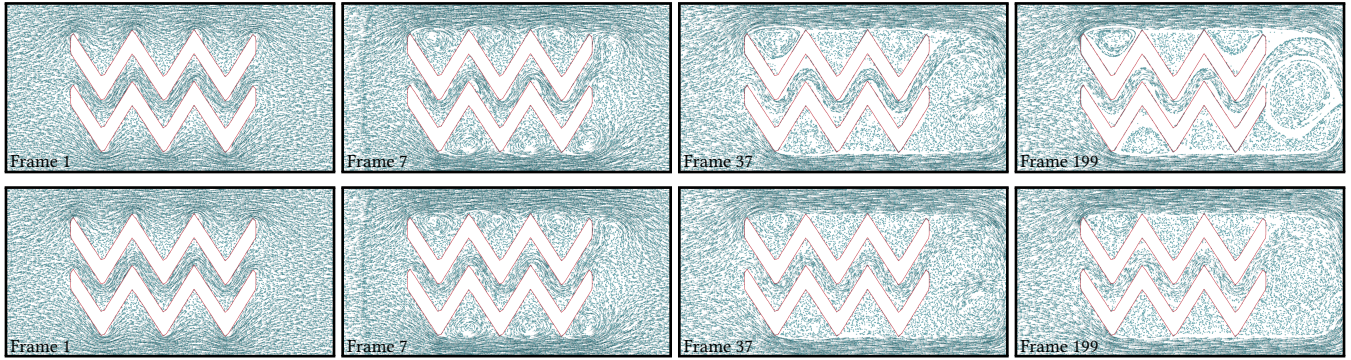


Fig. 16. **Jagged Obstacle Comparison:** Top: Particle trajectories under a time-dependent horizontal flow with jagged solid objects using bilinear direct velocity interpolation. Divergence near solids creates gaps in the flow in corners and downstream. Bottom: Particle trajectories under a horizontal flow with jagged solid objects using our Curl-Flow interpolation. The particles flow incompressibly around all details of the shape, minimizing the creation of gaps.

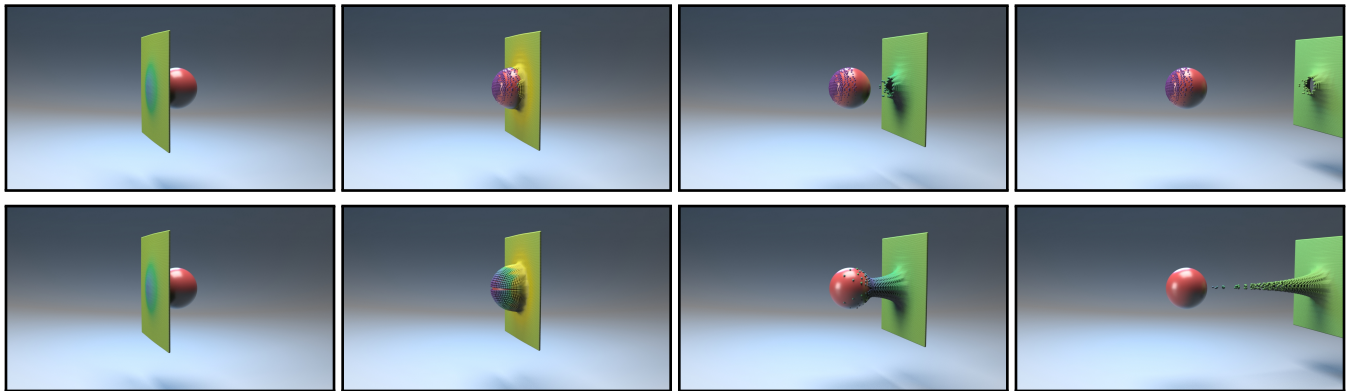


Fig. 17. **Smooth Obstacle Comparison in 3D:** Top row: Trilinear velocity interpolation causes many particle collisions with the solid. (Particles are frozen on contact.) Bottom row: Ramping out the normal velocity as particles approach the boundary yields almost ideal boundary behavior, although it introduces some velocity divergence.

the obstacle, leaving a gap in the flow. With our ramped-normal-velocity correction, we see that the particles instead flow smoothly around the obstacle without getting stuck.

To evaluate a somewhat higher resolution scenario, we use a G-shape obstacle on a $50 \times 50 \times 50$ grid and use an applied external force to create an intermittent upward impulse on a region of passive particles (Figure 18). Once again freezing particles at the time of collision, we see far more getting stuck in the direct velocity interpolation case than for Curl-Flow with our boundary correction.

To benchmark our scheme, we simulated 300 frames of the above 3D scenario on a 2.8 GHz Intel Core i7 processor listing the computation time for each simulation component in Table 1. Of the 353s spent on recovering the discrete ψ , by far the dominant cost is solving the scalar Poisson equation (348.83s) to correct the gauge, which was about half ($\sim 0.56\times$) the time for pressure projection. The time cost for parallel sweeping is comparatively insignificant (4.0177s). Advecting the maximum of 80K passive particles in this scenes takes more ($\sim 1.41\times$) time in our Curl-Flow method vs. direct trilinear velocity interpolation. This is because we used the slightly more computationally expensive quadratic kernels and must pay the extra cost of ramping near boundaries.

Our method plugs conveniently into a standard grid-based fluid solver. As our data indicates, the additional overhead of our method lies primarily in constructing smooth discrete vector potential fields from the face velocity data and using adapted interpolants. Although significantly less costly than the vector Poisson solve in some prior work [Ando et al. 2015], the most significant cost of our method still comes from solving the scalar Poisson equation (21) to enforce the Coulomb gauge condition in 3D. Our prototype used a basic conjugate gradient method, and thus there is significant opportunity to drive down this cost using the wide array of numerical methods designed for grid-based Poisson problems.

The actual interpolation procedures (as opposed to ψ reconstruction) could theoretically become the bottleneck if the particle count becomes massive. However, since such comparatively large passive particle counts are most often of value just for rendering, tracing particles can be done as an offline and highly parallel post-process after the dynamic simulation is already complete.

Naturally, optimization opportunities such as those mentioned above exist at various levels of abstraction, for our interpolants generally and our particular simulator implementation specifically. However, at a fundamental level, it is clear that the dominant extra costs of our framework will generally be one additional Poisson solve (comparable to the cost of the existing pressure projection) combined with slightly different (but still largely standard) interpolants. The decision to make this cost-quality tradeoff will be application-dependent, but we consider it worthwhile for scenarios where particle density and boundary fidelity are paramount.

7 CONCLUSIONS AND FUTURE WORK

Large time steps in particle trajectory integration, poorly enforced boundaries, and (optionally) inadequate pressure solver tolerances have long been known to cause density/volume drift in grid-based fluid animation; accordingly, a host of post-compensation strategies have been developed [Ando et al. 2012; Kugelstadt et al. 2019;

Sato et al. 2018b; Takahashi and Lin 2019]. However, we believe our work is the first in computer graphics to identify divergent velocity interpolation as another key factor. Our Curl-Flow interpolation framework, tailored to plug into popular grid-based cut-cell fluid animation tools, addresses this issue by globally guaranteeing pointwise divergence-free velocities. The resulting flows offer better long-term particle distributions and natural motions around obstacles. We believe our work opens a previously unexplored dimension in the design of advection schemes for fluid animation; our method's current limitations suggest exciting questions for investigation.

We considered only static obstacles. It is straightforward to support non-zero boundary fluxes during vector potential reconstruction; however, the Lagrangian nature of obstacle motion raises intriguing questions about collision-safe time integration of trajectories, especially for intermediate substeps of Runge-Kutta. A deforming mesh strategy that carries the potential with it is a possible avenue. Similarly, we have only discussed grid domains that are either fully open, fully closed, or "wind-tunnel"-like. More general boundary conditions would be an obvious extension, including free surface boundaries for liquid animation where our method could improve volume conservation.

We focused on the effects of incompressible interpolation on passive particle trajectories. However, our stronger enforcement of the continuity equation might also offer visual benefits for advection of the velocity field itself and/or grid-based scalar fields like temperature or density.

A minor drawback of Curl-Noise-based boundary treatment (both Bridson's and our variant) is that, though always incompressible, it yields tangential velocity discontinuities where the distance field is nonsmooth, i.e., near concave corners. Our simple velocity-based 3D boundary correction can similarly suffer from discontinuities in such regions.

We experimented with a few strictly divergence-free 3D boundary correction strategies based on matrix-valued RBFs [McNally 2011] and panel methods used in vorticity schemes [Park and Kim 2005]. Although smooth and divergence-free, they require costly global solves and are less precise than our (potentially divergent) 3D velocity ramping-based approach. The development of an efficient, artifact- and divergence-free ramping-type solution in 3D based on vector potentials would be valuable, but is complicated by discontinuous mesh normals [Bridson et al. 2007] and interactions among ψ components.

Lastly, because of the high cost and limited controllability of fluid simulations, the ability to edit simulations in an *efficient* post-process would also be valuable [Pan et al. 2013; Sato et al. 2018a]. Our Curl-Noise (vector potential) boundary correction in 2D suggests that the use of vector potentials may enable other fast, divergence-free editing capabilities, beyond basic turbulent noise [Kim et al. 2008], by exploiting the compatibility of Curl-Noise's vector potential-based *procedural* tools with our (and others') vector potential-based *simulation* tools.

REFERENCES

- R. Albanese and G. Rubinacci. 1990. Magnetostatic field computations in terms of two-component vector potentials. *Internat. J. Numer. Methods Engrg.* 29, 3 (mar 1990), 515–532. <https://doi.org/10.1002/nme.1620290305>

Interpolation method	Pressure projection	SL velocity advection	Particle advection	Discrete ψ construction	Total time (s)
Direct velocity interpolation	629.17	1437.8	153.96	-	2223.0
Curl-Flow	634.30	1437.0	216.37	353.09	2643.2

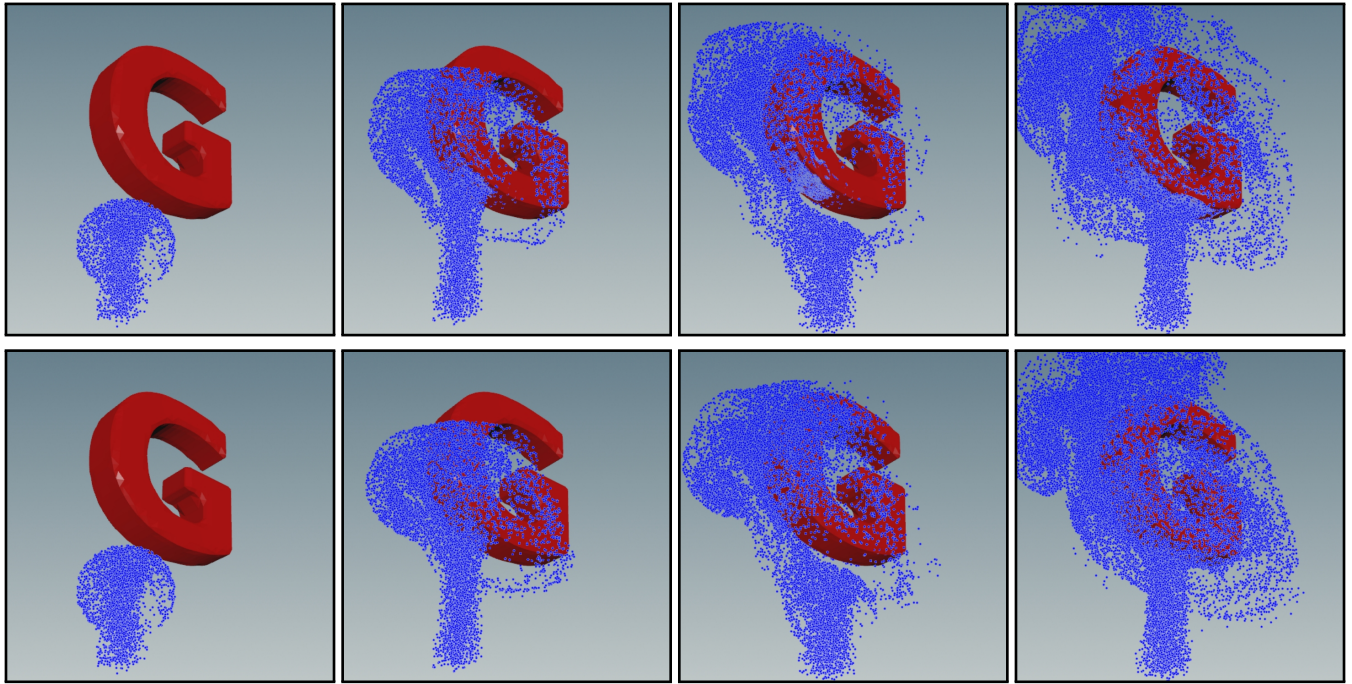
Table 1. Computational Time Comparison for 300 frames of the 50^3 grid simulation in Figure 18.

Fig. 18. **Dynamic Flow Past An Obstacle in 3D** : Top row: Trilinear velocity interpolation causes many particle collisions at the bottom left of the G-shape. (Particles are frozen on contact for illustration.) Bottom row: Ramping out the normal velocity as particles approach the boundary yields almost ideal boundary behavior, although it introduces some velocity divergence.

Ryoichi Ando, Nils Thuerey, and Chris Wojtan. 2015. A stream function solver for liquid simulations. *ACM Transactions on Graphics* 34, 4 (jul 2015), 53:1–53:9. <https://doi.org/10.1145/2766935>

Ryoichi Ando, Nils Thuerey, and Reiji Tsuruno. 2012. Preserving fluid sheets with adaptively sampled anisotropic particles. *IEEE transactions on visualization and computer graphics* 18, 8 (2012), 1202–1214.

Alexis Angelidis and Fabrice Neyret. 2005. Simulation of smoke based on vortex filament primitives. In *Proceedings of the 2005 ACM SIGGRAPH/Eurographics symposium on Computer animation*. ACM, 87–96.

Vinicius C Azevedo, Christopher Batty, and Manuel M Oliveira. 2016. Preserving geometry and topology for fluid flows with thin obstacles and narrow gaps. *ACM Transactions on Graphics (TOG)* 35, 4 (2016), 97.

Dinshaw S Balsara. 2001. Divergence-free adaptive mesh refinement for magnetohydrodynamics. *J. Comput. Phys.* 174, 2 (2001), 614–648.

Dinshaw S Balsara. 2004. Second-order-accurate schemes for magnetohydrodynamics with divergence-free reconstruction. *The Astrophysical Journal Supplement Series* 151, 1 (2004), 149.

Dinshaw S Balsara. 2009. Divergence-free reconstruction of magnetic fields and WENO schemes for magnetohydrodynamics. *J. Comput. Phys.* 228, 14 (2009), 5040–5056.

Yuanxun Bao, Aleksandar Donev, Boyce E Griffith, David M McQueen, and Charles S Peskin. 2017. An Immersed Boundary method with divergence-free velocity interpolation and force spreading. *Journal of computational physics* 347 (2017), 183–206.

Christopher Batty, Florence Bertails, and Robert Bridson. 2007. A fast variational framework for accurate solid-fluid coupling. *ACM Trans. Graph.* 26, 3 (2007), 100.

Ayan Biswas, Richard Strelitz, Jonathan Woodring, Chun-Ming Chen, and Han-Wei Shen. 2016. A scalable streamline generation algorithm via flux-based isocontour extraction. In *Proceedings of the 16th Eurographics Symposium on Parallel Graphics*

and Visualization. 69–78.

R. Bridson. 2015. *Fluid Simulation for Computer Graphics, Second Edition*. Taylor & Francis.

Robert Bridson, Jim Houriham, and Marcus Nordenstam. 2007. Curl-Noise for Procedural Fluid Flow. *ACM Trans. Graph.* 26, 3 (July 2007), 46–es. <https://doi.org/10.1145/1276377.1276435>

Tyson Brochu, Todd Keeler, and Robert Bridson. 2012. Linear-time smoke animation with vortex sheet meshes. In *Proceedings of the ACM SIGGRAPH/Eurographics Symposium on Computer Animation*. Eurographics Association, 87–95.

Bernardo Cockburn, Fengyan Li, and Chi-Wang Shu. 2004. Locally divergence-free discontinuous Galerkin methods for the Maxwell equations. *J. Comput. Phys.* 194, 2 (2004), 588–610.

Qiaodong Cui, Pradeep Sen, and Theodore Kim. 2018. Scalable laplacian eigenfluids. *ACM Transactions on Graphics (TOG)* 37, 4 (2018), 87.

Fang Da, Christopher Batty, Chris Wojtan, and Eitan Grinspun. 2015. Double bubbles sans toil and trouble: Discrete circulation-preserving vortex sheets for soap films and foams. *ACM Transactions on Graphics (TOG)* 34, 4 (2015), 149.

Fang Da, David Hahn, Christopher Batty, Chris Wojtan, and Eitan Grinspun. 2016. Surface-only liquids. *ACM Transactions on Graphics (TOG)* 35, 4 (2016), 1–12.

Tyler De Witt, Christian Lessig, and Eugene Fiume. 2012. Fluid simulation using Laplacian eigenfunctions. *ACM Transactions on Graphics (TOG)* 31, 1 (2012), 10.

Ivan DeWolf. 2006. *Divergence-free noise*. Technical Report. Technical report, Martian Labs., 2005.

Marvin Eisenberger, Zorah Löhner, and Daniel Cremers. 2018. Divergence-Free Shape Interpolation and Correspondence. *arXiv preprint arXiv:1806.10417* (2018).

Sharif Elcott, Yiying Tong, Eva Kanso, Peter Schröder, and Mathieu Desbrun. 2007. Stable, circulation-preserving, simplicial fluids. *ACM Transactions on Graphics (TOG)*

- 26, 1 (2007), 4.
- Douglas Enright, Stephen Marschner, and Ronald Fedkiw. 2002. Animation and rendering of complex water surfaces. *ACM Transactions on Graphics (TOG)* 21, 3 (2002), 736–744.
- John A Evans and Thomas JR Hughes. 2013. Isogeometric divergence-conforming B-splines for the unsteady Navier–Stokes equations. *J. Comput. Phys.* 241 (2013), 141–167.
- Ronald Fedkiw, Jos Stam, and Henrik Wann Jensen. 2001. Visual Simulation of Smoke. In *Proceedings of the 28th Annual Conference on Computer Graphics and Interactive Techniques (SIGGRAPH '01)*. ACM, New York, NY, USA, 15–22. <https://doi.org/10.1145/383259.383260>
- F. N. Fritsch and R. E. Carlson. 1980. Monotone Piecewise Cubic Interpolation. *SIAM J. Numer. Anal.* 17, 2 (1980), 238–246.
- Ben Houston, Chris Bond, and Mark Wiebe. 2003. A unified approach for modeling complex occlusions in fluid simulations. In *ACM SIGGRAPH 2003 Sketches & Applications*. 1–1.
- Antonio Huerta, Yolanda Vidal, and Pierre Villon. 2004. Pseudo-divergence-free element free Galerkin method for incompressible fluid flow. *Computer Methods in Applied Mechanics and Engineering* 193, 12 (2004), 1119–1136. <https://doi.org/10.1016/j.cma.2003.12.010> Meshfree Methods: Recent Advances and New Applications.
- P Jenny, SB Pope, M Muradoglu, and DA Caughey. 2001. A hybrid algorithm for the joint PDF equation of turbulent reactive flows. *J. Comput. Phys.* 166, 2 (2001), 218–252.
- Chenfanfu Jiang, Craig Schroeder, Andrew Selle, Joseph Teran, and Alexey Stomakhin. 2015. The affine particle-in-cell method. *ACM Transactions on Graphics (TOG)* 34, 4 (2015), 51.
- Chenfanfu Jiang, Craig Schroeder, Joseph Teran, Alexey Stomakhin, and Andrew Selle. 2016. The material point method for simulating continuum materials. In *ACM SIGGRAPH 2016 Courses*. 1–52.
- Theodore Kim, Nils Thürey, Doug James, and Markus Gross. 2008. Wavelet Turbulence for Fluid Simulation. *ACM Trans. Graph.* 27, 3 (Aug. 2008), 1–6. <https://doi.org/10.1145/1360612.1360649>
- Tassilo Kugelschadt, Andreas Longva, Nils Thürey, and Jan Bender. 2019. Implicit Density Projection for Volume Conserving Liquids. *IEEE Computer Architecture Letters* 01 (2019), 1–1.
- Egor Larionov, Christopher Batty, and Robert Bridson. 2017. Variational stokes: a unified pressure-viscosity solver for accurate viscous liquids. *ACM Transactions on Graphics (TOG)* 36, 4 (2017), 101.
- Christoph Lehrenfeld and Joachim Schöberl. 2016. High order exactly divergence-free hybrid discontinuous Galerkin methods for unsteady incompressible flows. *Computer Methods in Applied Mechanics and Engineering* 307 (2016), 339–361.
- J.B. Manges and Z.J. Cendes. 1995. A generalized tree-cotree gauge for magnetic field computation. *IEEE Transactions on Magnetics* 31, 3 (may 1995), 1342–1347. <https://doi.org/10.1109/20.376275>
- Colin P McNally. 2011. Divergence-free interpolation of vector fields from point values—exact $\text{div-B} = 0$ in numerical simulations. *Monthly Notices of the Royal Astronomical Society: Letters* 413, 1 (2011), L76–L80.
- DW Meyer and P Jenny. 2004. Conservative velocity interpolation for PDF methods. In *PAMM: Proceedings in Applied Mathematics and Mechanics*, Vol. 4. Wiley Online Library, 466–467.
- Yen Ting Ng, Chohong Min, and Frédéric Gibou. 2009. An Efficient Fluid-solid Coupling Algorithm for Single-phase Flows. *J. Comput. Phys.* 228, 23 (Dec. 2009), 8807–8829.
- Zherong Pan, Jin Huang, Yiyong Tong, Changxi Zheng, and Hujun Bao. 2013. Interactive localized liquid motion editing. *ACM Transactions on Graphics (TOG)* 32, 6 (2013), 1–10.
- Sang Il Park and Myoung Jun Kim. 2005. Vortex fluid for gaseous phenomena. In *Proceedings of the 2005 ACM SIGGRAPH/Eurographics symposium on Computer animation*. ACM, 261–270.
- Charles S Peskin. 2002. The immersed boundary method. *Acta numerica* 11 (2002), 479–517.
- Tobias Pfaff, Nils Thürey, and Markus Gross. 2012. Lagrangian vortex sheets for animating fluids. *ACM Transactions on Graphics (TOG)* 31, 4 (2012), 112.
- Konstantin Poelke and Konrad Polthier. 2016. Boundary-aware Hodge decompositions for piecewise constant vector fields. *Computer-Aided Design* 78 (2016), 126–136.
- Adina E Pusok, Boris JP Kaus, and Anton A Popov. 2017. On the quality of velocity interpolation schemes for marker-in-cell method and staggered grids. *Pure and Applied Geophysics* 174, 3 (2017), 1071–1089.
- Nick Rasmussen, Douglas Enright, Duc Nguyen, Sebastian Marino, Nigel Sumner, Willi Geiger, Samir Hoon, and Ronald Fedkiw. 2004. Directable photorealistic liquids. In *Proceedings of the 2004 ACM SIGGRAPH/Eurographics symposium on Computer animation*. 193–202.
- Bharath Ravu, Murray Rudman, Guy Metcalfe, Daniel Lester, and Devang Khakhar. 2016. Creating analytically divergence-free velocity fields from grid-based data. *J. Comput. Phys.* 323 (07 2016). <https://doi.org/10.1016/j.jcp.2016.07.018>
- Sander Rhebergen and Garth N Wells. 2018. A hybridizable discontinuous Galerkin method for the Navier–Stokes equations with pointwise divergence-free velocity field. *Journal of Scientific Computing* 76, 3 (2018), 1484–1501.
- Syuhei Sato, Yoshinori Dobashi, and Tomoyuki Nishita. 2018a. Editing fluid animation using flow interpolation. *ACM Transactions on Graphics (TOG)* 37, 5 (2018), 1–12.
- Syuhei Sato, Yoshinori Dobashi, Yonghao Yue, Kei Iwasaki, and Tomoyuki Nishita. 2015. Incompressibility-preserving deformation for fluid flows using vector potentials. *The Visual Computer* 31, 6 (2015), 959–965.
- Takahiro Sato, Christopher Wojtan, Nils Thürey, Takeo Igarashi, and Ryoichi Ando. 2018b. Extended narrow band FLIP for liquid simulations. In *Computer Graphics Forum*, Vol. 37. Wiley Online Library, 169–177.
- Hagit Schechter and Robert Bridson. 2008. Evolving sub-grid turbulence for smoke animation. In *Proceedings of the 2008 ACM SIGGRAPH/Eurographics symposium on Computer animation*. Eurographics Association, 1–7.
- Andrew Selle, Ronald Fedkiw, Byungmoon Kim, Yingjie Liu, and Jarek Rossignac. 2008. An unconditionally stable MacCormack method. *Journal of Scientific Computing* 35, 2-3 (2008), 350–371.
- Zachary J. Silberman, Thomas R. Adams, Joshua A. Faber, Zachariah B. Etienne, and Ian Ruchlin. 2019. Numerical generation of vector potentials from specified magnetic fields. *J. Comput. Phys.* 379 (2019), 421–437. <https://doi.org/10.1016/j.jcp.2018.12.006>
- Jos Stam. 1999. Stable Fluids. In *Proceedings of the 26th Annual Conference on Computer Graphics and Interactive Techniques (SIGGRAPH '99)*. ACM Press/Addison-Wesley Publishing Co., New York, NY, USA, 121–128. <https://doi.org/10.1145/311535.311548>
- Jos Stam and Eugene Fiume. 1993. Turbulent wind fields for gaseous phenomena. In *Proceedings of the 20th annual conference on Computer graphics and interactive techniques*. 369–376.
- Michael Steffen, Robert M Kirby, and Martin Berzins. 2008. Analysis and reduction of quadrature errors in the material point method (MPM). *International journal for numerical methods in engineering* 76, 6 (2008), 922–948.
- Tetsuya Takahashi and Ming C Lin. 2019. A geometrically consistent viscous fluid solver with two-way fluid-solid coupling. In *Computer Graphics Forum*, Vol. 38. Wiley Online Library, 49–58.
- Yiyong Tong, Santiago Lombeyda, Anil N Hirani, and Mathieu Desbrun. 2003. Discrete multiscale vector field decomposition. *ACM transactions on graphics (TOG)* 22, 3 (2003), 445–452.
- Wolfram Von Funck, Holger Theisel, and Hans-Peter Seidel. 2006. Vector field based shape deformations. In *ACM Transactions on Graphics (TOG)*, Vol. 25. ACM, 1118–1125.
- Hongliang Wang, Roberto Agrusta, and Jeroen van Hunen. 2015. Advantages of a conservative velocity interpolation (CVI) scheme for particle-in-cell methods with application in geodynamic modeling. *Geochemistry, Geophysics, Geosystems* 16, 6 (2015), 2015–2023.
- Rundong Zhao, Mathieu Desbrun, Guo-Wei Wei, and Yiyong Tong. 2019. 3D Hodge decompositions of edge- and face-based vector fields. *ACM Transactions on Graphics (TOG)* 38, 6 (2019), 1–13.
- Yongning Zhu and Robert Bridson. 2005. Animating sand as a fluid. *ACM Transactions on Graphics (TOG)* 24, 3 (2005), 965–972.